J. Fluid Mech. (1989), *vol.* 200, *pp.* 39–67
Printed in Great Britain

Dynamic simulation of bounded suspensions of hydrodynamically interacting particles

By LOUIS J. DURLOFSKY† AND JOHN F. BRADY‡

† Chevron Oil Field Research Company, PO Box 446, La Habra, CA 90633–0446, USA

‡ Department of Chemical Engineering, California Institute of Technology,
Pasadena, CA 91125, USA

(Received 5 January 1988)

A general method for computing the hydrodynamic interactions among an infinite suspension of particles immersed between two infinite plane boundaries, under the condition of vanishing particle Reynolds number, is presented. The method accounts for both near-field particle–particle and particle–boundary lubrication effects as well as dominant many-body effects, which include reflections with both particles and boundaries. Through relative motion of the boundaries, a bulk shear flow can be generated, and the resulting particle motions, as well as the forces exerted by the boundaries on the fluid, computed. Knowledge of the boundary forces allows for the calculation of the suspension viscosity. The simulation method is applied to several example problems; in one, the resuspension of a sediment layer of particles is illustrated. The general method can also be extended to dynamically simulate suspensions immersed in a pressure driven flow between two walls or through a tube.

1. Introduction

Dynamic simulation is a powerful tool in the study of suspensions of particles interacting hydrodynamically in the Stokes' flow regime. Through simulation, macroscopic suspension properties, such as effective viscosity, sedimentation rate or self-diffusion coefficient are determined through appropriate temporal and spatial averages of microstructural information, elucidating the relationship between behaviour on the two lengthscales. In cases where a statistically homogeneous microstructure exists (e.g. an unbounded suspension with no large-scale variations), a portion of the suspension far removed from any physical boundaries can be considered, and the direct effect of the boundaries on the system removed. In statistically homogeneous systems where boundary motion is necessary to drive a flow, for example in the case of particles immersed in an unbounded shear flow, the flow field is simply mathematically imposed, with no specification of its origin.

Direct boundary effects are, however, often important in Stokes' flow problems. Due to the slow decay of the disturbances produced by the particles, and to the great extent of the boundaries, boundary interactions can have a quantitative effect on the behaviour of isolated particles or dilute suspensions. In more concentrated systems, however, the presence of boundaries can have an even more significant effect, in some cases qualitatively altering the suspension behaviour. For example, because of the tendency of sheared suspensions to form clusters, whose characteristic size grows with increasing volume fraction of solids, at sufficiently high volume fractions percolating clusters that span the gap between moving plates may form, resulting in a flow which is boundary dominated and therefore not statistically homogeneous. In such an instance the actual boundary must be treated directly, i.e. included in the dynamic simulation method.

The purpose of this paper is to present a simulation method capable of describing the motions of particles immersed in a fluid bounded by plane walls under conditions of vanishing particle Reynolds number. The method is general and can be applied to a variety of bounded suspension problems, though our emphasis will be on the problem of a suspension of force- and torque-free spheres subjected to shear. The shear derives from the relative motion of the two boundaries, which are assumed to be planes infinite in extent.

In an earlier paper (Durlofsky, Brady & Bossis 1987), a general method for the dynamic simulation of finite systems of hydrodynamically interacting particles was presented. This method employs a moment expansion of the integral representation for the Stokes' flow velocity field, in conjunction with Faxén laws, to yield a far-field approximation to the many-body mobility matrix. (Recall that the mobility matrix relates the particle velocities to the forces and torques they exert on the fluid.) Inversion of this mobility matrix results in a far-field approximation to the resistance matrix, which contains the dominant many-body effects. Near-field lubrication effects are introduced into the resistance matrix in a pairwise manner via the exact two-body results. The method has been extended to infinite, statistically homogeneous systems by Brady, Phillips, Lester & Bossis (1988) through application of the method of O'Brien (1979) and the Ewald summation technique.

Both the many-body and lubrication effects included in the resistance matrix result in important macroscopic behaviour in unbounded systems. The many-body interactions reproduce the 'effective medium' aspects of suspensions, such as the screening characteristic of porous media (Durlofsky & Brady 1987), while the lubrication interactions, in addition to preventing particle overlap during the course of a dynamic simulation, are essential to the formation of large clusters, which result in large effective viscosities (Bossis & Brady 1984; Brady & Bossis 1985).

The method developed in this paper for bounded systems of hydrodynamically interacting particles contains elements of the methods of both Durlofsky *et al.* and Brady *et al.* As in both these methods, the starting point here is the general integral form of the Stokes' flow velocity field, applied to both the suspension particles and the bounding plane walls. The walls are divided into two regions: a near region, which is discretized into a finite number of wall patches that interact with one another, as well as with all the suspended particles, in the mobility matrix, and a far region, whose average integrated effect on the motion of the particles and wall patches is calculated analytically. The effects of the far region are somewhat analogous to the 'back-flow' integrals discussed by Brady *et al.*

Near-field two-sphere interactions are included as in Durlofsky *et al.* Near-field sphere–wall interactions are introduced through use of exact sphere–wall solutions. The resulting resistance matrix, therefore, contains both many-body effects, with reflections both with particles and with the wall patches, and near-field singular lubrication effects. Particle velocities are determined by solving a matrix equation and trajectories tracked by integrating these velocities in time.

Many previous investigators have considered the problem of particle motion near one or between two plane walls in Stokes' flow. The early far-field asymptotic solutions for one sphere near a single plane wall or between two plane walls computed by Faxén and others are discussed by Happel & Brenner (1973). Exact solutions now exist for the general motion of a single sphere near a single plane wall with the fluid at infinity quiescent (Brenner 1961; Maude 1961; Goldman, Cox & Brenner 1967*a*; Dean & O'Neill 1963; O'Neill 1964) as do near-field asymptotic results (Cox & Brenner 1967; Goldman, Cox & Brenner 1967*a*; O'Neill & Stewartson 1967). The more general problem involving sphere motion near a plane wall subject to an imposed shear flow has also been solved (Goldman, Cox & Brenner 1967*b*; O'Neill 1968).

No exact analytic solutions exist for the motion of two spheres near a single plane wall or for one sphere between two plane walls. The most complete far-field solutions to date for the two-plane problem are those of Ho & Leal (1974) who considered the inertial migration of spheres in unidirectional flows. An extensive numerical study of the two-plane problem was performed by Ganatos, Pfeffer & Weinbaum (1980*a*) and Ganatos, Weinbaum & Pfeffer (1980*b*, 1982). Using a boundary collocation method, these investigators computed translational and rotational velocities for force- and torque-free spheres immersed in either Couette or Poiseuille flow, as well as forces exerted by spheres translating parallel or perpendicular to the walls. These solutions are extremely accurate and will serve as a check on the accuracy of our method. The boundary collocation method employed, however, is computationally intensive and would result in prohibitive computation times if applied to the complex many-particle systems we wish to consider. For further discussion of this point see Durlofsky *et al.* 1987.

In §2 we develop the general simulation method for either a finite or an infinite system of identical spheres bounded between two plane walls. Beginning with the integral formulation for Stokes' flow, we form a far-field approximation to the grand mobility matrix. The effect of the planes in the far-region, i.e. the non-discretized portion, is discussed in detail for the case of shear flow. Next, the adjustments made to the invert of the mobility matrix, which result in a resistance matrix containing both many-body and near-field lubrication effects, are considered. Then, it will be seen that by prescribing the walls to translate uniformly, both sphere velocities and the forces exerted by the walls on the fluid can be computed. Knowledge of the wall forces allows for calculation of both the effective viscosity and any normal stress differences that may be present. In §3 we compare our results for one sphere between two plane walls with the results of Ganatos *et al.* (1980*a*, 1980*b*, 1982). These comparisons illustrate the accuracy of the general method. Next, a model problem involving the motion of six nearly touching spheres aligned along the compressional shear flow axis is discussed. This example illustrates the ability of the method to handle sensitive configurations and demonstrates that lubrication forces are modelled correctly.

Two examples that more clearly demonstrate the capabilities of the general method are presented in §4. These examples involve suspensions confined within a monolayer oriented between the two planes, i.e. the sphere centres all lie in a plane perpendicular to the physical boundaries. Such monolayer simulations result in considerable computational savings while generally retaining the essential physics. The first example is a simulation displaying the resuspension of a system of spheres initially located near the bottom plane. This phenomenon, called viscous resuspension, has been observed experimentally by Gadala-Maria (1979) and Leighton & Acrivos (1986). Next, we present simulation results for a moderately dilute suspension of force- and torque-free spheres subject to shear. These results display the types of long-time behaviour and time-average quantities observable via dynamic simulation, e.g. viscosity, particle distribution functions and particle average velocities. Finally, we conclude by providing some results from a more complete study of the behaviour of concentrated suspensions under shear, which will be the subject of a subsequent publication. We also discuss other types of problems that can be studied within the same general framework.

2. Simulation method

In this section we shall develop a method to simulate the dynamics of either a finite or an infinite number of rigid particles confined between two plane walls. Particle motion results from relative motion of the walls, which generates a flow, as well as, in the case of a finite number of particles, through imposed particle forces and torques. The particles are assumed to be small enough such that the particle Reynolds number, Ua/ν, where U is a characteristic particle velocity, a a characteristic particle size and ν the kinematic viscosity of the fluid, is much less than unity.

In unbounded Stokes' flow problems, owing to the linearity of the governing equations, the velocities of all the particles can be related to the forces and torques exerted on the fluid by each of the particles via the mobility matrix $\boldsymbol{M}$:

$$U - \boldsymbol{u}^{\infty} = \boldsymbol{M} \cdot \boldsymbol{F}, \tag{2.1}$$

where $\boldsymbol{U}$ is a generalized velocity vector, $\boldsymbol{u}^{\infty}$ is the velocity field in the absence of the particles and $\boldsymbol{F}$ is a generalized force vector. The inverse problem involves the resistance matrix $\boldsymbol{R}$:

$$\boldsymbol{F} = \boldsymbol{R} \cdot (U - \boldsymbol{u}^{\infty}), \tag{2.2}$$

with $\boldsymbol{M}$ and $\boldsymbol{R}$ related through an inversion

$$\boldsymbol{R} = \boldsymbol{M}^{-1}. \tag{2.3}$$

Both $\boldsymbol{M}$ and $\boldsymbol{R}$ are purely geometric entities, depending only on the instantaneous particle configuration and not on the velocities or forces imposed on the particles. As we shall see, relations very similar to (2.1) and (2.2) will be applicable to bounded Stokes' flow problems. The integrated effect of the walls outside the discretized region acts much like an imposed flow; designating this effect $\boldsymbol{B}$, (2.1) is now of the form

$$U = \boldsymbol{M} \cdot \boldsymbol{F} + \boldsymbol{B}. \tag{2.4}$$

Before proceeding with the formulation of our method, let us briefly consider two alternative approaches. As discussed in §1, the method formulated here for determining $\boldsymbol{M}$ and $\boldsymbol{R}$ for bounded suspensions proceeds from the integral representation for the Stokes' flow velocity field, which is in terms of the free-space Green function or fundamental solution, known also as the Stokeslet. This approach requires that a portion of the bounding planes be discretized in order that the particles interact both directly and indirectly with the boundaries. Two alternative approaches are also possible however. In one, the need to discretize a portion of the bounding plane walls is eliminated, while in the other only a portion of one plane need be discretized. The first approach, which requires no wall discretization, begins with the fundamental solution for Stokes' flow between two parallel plane walls, as given by Liron & Mochon (1976). By performing a moment expansion of their expression, sphere interactions can be formed which explicitly include the presence of the walls. Their expression is, however, in terms of an infinite series, which is computationally expensive to evaluate. And further, exact two-sphere solutions, which we require to build lubrication into the resistance matrix, are not yet available for two spheres between two infinite plane boundaries. The second alternative approach begins with the fundamental solution for a sphere near a single plane wall (Blake 1971), which, unlike the fundamental solution for a point force between two walls, is inexpensive to evaluate. In this case, however, only the second boundary need be discretized. Unfortunately, as was the case with the first alternative method, the exact solutions for two spheres near a single plane boundary are not yet available. Though these solutions could be approximated, we chose to approach the problem through the integral representation for the velocity field in terms of the free-space Green function, where exact two-sphere solutions are known. Our method, therefore, requires a portion of both walls to be discretized. Through this approach generality is retained – the method can easily handle, for example, particle motion near finite plane boundaries or through conduits, while the approaches described above cannot. Possible computational savings that might be realized by the two alternative approaches are discussed below.

In all that follows, the plane boundaries will be assumed to lie in the (x,z)-planes of a rectangular coordinate system, with the spacing between them designated H. To simulate a suspension of infinite extent, periodic boundary conditions will be applied in the x- and z-directions. The volume fraction of spheres, ϕ, is given by

$$\phi = \frac{\frac{4}{3}\pi a^3 N}{H L_x L_z}, \tag{2.5}$$

where a is the sphere radius, N is the number of spheres in the periodic cell and L_x and L_z are the lengths of the periodic cell in the x- and z-directions.

2.1. *Grand mobility matrix*

The formation of the grand mobility matrix will now be considered. The equation set is of a form similar to that for finite systems of spheres, with additional terms to account for the walls. Interactions between spheres in the mobility matrix are precisely as in Durlofsky *et al.* 1987. Specifically, the integral representation for the Stokes' flow velocity field is expanded in the moments of the force distribution about the sphere centre in conjunction with Faxén laws for the particle velocities. Moments are retained up to the desired order of accuracy. In the present problem, the force (zeroth moment), torque (antisymmetric part of the first moment) and stresslet (symmetric part of the first moment) are retained, yielding sphere–sphere mobility interactions accurate to $O(r^{-5})$, where r is a characteristic interparticle spacing.

Introducing the boundary interactions into the formulation, the equation set for a periodically replicated system of N spheres and P wall patches is:

$$\begin{bmatrix} \boldsymbol{U} \\ -\boldsymbol{E} \\ \boldsymbol{V} \end{bmatrix} = \begin{bmatrix} \boldsymbol{M}_{UF} & \boldsymbol{M}_{US} & \boldsymbol{M}_{UT} \\ \boldsymbol{M}_{EF} & \boldsymbol{M}_{ES} & \boldsymbol{M}_{ET} \\ \boldsymbol{M}_{VF} & \boldsymbol{M}_{VS} & \boldsymbol{M}_{VT} \end{bmatrix} \cdot \begin{bmatrix} \boldsymbol{F} \\ \boldsymbol{S} \\ \boldsymbol{T} \end{bmatrix} + \begin{bmatrix} \boldsymbol{B}_U \\ \boldsymbol{B}_E \\ \boldsymbol{B}_V \end{bmatrix}, \tag{2.6}$$

where $\boldsymbol{U}$ is a vector of dimension $6N$ containing the translational and rotational velocities of the spheres, $\boldsymbol{E}$ (of dimension $5N$) is the bulk rate of strain (which is zero for bounded systems), $\boldsymbol{V}$ (of dimension $3P$) contains the velocities of the wall patches, $\boldsymbol{F}$ (of dimension $6N$) contains the forces and torques exerted by the spheres on the fluid, $\boldsymbol{S}$ (of dimension $5N$) contains the stresslets exerted by the spheres on the fluid, $\boldsymbol{T}$ (of dimension $3P$) contains the forces exerted by the wall patches on the fluid and $\boldsymbol{B}_U$, $\boldsymbol{B}_E$ and $\boldsymbol{B}_V$, to be considered in detail below, contain the integrated effect of the wall outside the discretized region, as well as a portion of the effect of the wall patches. Note that the force density on the surface of a wall patch is approximated directly and not, as for the spheres, expanded in moments; thus there are no torque or stresslet unknowns associated with the wall patches. The submatrices $\boldsymbol{M}_{UF}$, $\boldsymbol{M}_{US}$, $\boldsymbol{M}_{EF}$ and $\boldsymbol{M}_{ES}$ comprise the grand mobility matrix $\mathscr{M}$ for a finite system of spheres in an unbounded fluid. The grand mobility matrix in the problem at hand, of dimension $11N+3P$, containing all nine submatrices, will be designated $\mathscr{M}^{\mathrm{W}}$.

To derive expressions for the components of $\mathscr{M}^{\mathrm{W}}$, we begin with the integral representation for the Stokes' flow solution (Ladyzhenskaya 1963):

$$u_i(\boldsymbol{x}) - u_i^{\infty}(\boldsymbol{x}) = -\frac{1}{8\pi\eta}\int_S J_{ij} f_j \,\mathrm{d}S + \frac{3}{4\pi}\int_S K_{ijk}\, u_j n_k \,\mathrm{d}S \quad (\boldsymbol{x} \notin S), \tag{2.7a}$$

$$\tfrac{1}{2}u_i(\boldsymbol{x}) - u_i^{\infty}(\boldsymbol{x}) = -\frac{1}{8\pi\eta}\int_S J_{ij} f_j \,\mathrm{d}S + \frac{3}{4\pi}\int_S K_{ijk}\, u_j n_k \,\mathrm{d}S \quad (\boldsymbol{x} \in S), \tag{2.7b}$$

with

$$J_{ij} = \frac{\delta_{ij}}{r} + \frac{r_i r_j}{r^3}, \tag{2.7c}$$

$$K_{ijk} = \frac{r_i r_j r_k}{r^5}, \tag{2.7d}$$

where $\boldsymbol{x}$ is a field point in the fluid–particle–boundary continuum and $\boldsymbol{y}$ a point on a particle or boundary surface, $\boldsymbol{r} = \boldsymbol{x}-\boldsymbol{y}$, $r = |\boldsymbol{r}|$, f_j is the force density exerted by the fluid on the surface, n_k is the normal pointing from the surface into the fluid, $u_i(\boldsymbol{x})$ is the velocity at the point $\boldsymbol{x}$ and $u_i^{\infty}(\boldsymbol{x})$ is the imposed flow at infinity. Note that (2.7*a*) applies for a point in the fluid and (2.7*b*) applies for a point on a surface. The second integral on the right-hand side of (2.7*a*), upon application of the divergence theorem, vanishes for rigid particles that bound a volume, resulting in the following expression

$$u_i(\boldsymbol{x}) - u_i^{\infty}(\boldsymbol{x}) = -\frac{1}{8\pi\eta}\int_S J_{ij} f_j \,\mathrm{d}S. \tag{2.7e}$$

Equation (2.7*e*) is valid for all points $\boldsymbol{x}$, both in the fluid and on the surfaces that bound a volume (i.e. for rigid particles that bound a volume, both (2.7*a*) and (2.7*b*) reduce to (2.7*e*)). Thus, (2.7*e*) is the expression applicable to interacting spheres. Indeed, this equation is the starting point for systems of interacting spheres and yields the components of $\boldsymbol{M}_{UF}$, $\boldsymbol{M}_{US}$, $\boldsymbol{M}_{EF}$ and $\boldsymbol{M}_{ES}$. These matrices, formulated in detail in Durlofsky *et al.*, will not be considered further here.

Because the wall patches do not bound a volume, the divergence theorem cannot be applied to integrals over their surface, and the more general expressions (2.7*a*) and (2.7*b*) must be retained for interactions involving wall patches. Upon the assumption of constant force density over the surface of a wall patch, (2.7*a*) and (2.7*b*) become

$$u_i(\boldsymbol{x}) = \frac{1}{8\pi\eta}\frac{F_j^{\gamma}}{A_{\gamma}}\int_{S_{\gamma}} J_{ij}\,\mathrm{d}S + \frac{3}{4\pi}U_j^{\gamma}\int_{S_{\gamma}} K_{ijk}\, n_k \,\mathrm{d}S \quad (\boldsymbol{x} \notin S_{\gamma}), \tag{2.8a}$$

$$\tfrac{1}{2}U_i^{\gamma} = \frac{1}{8\pi\eta}\frac{F_j^{\gamma}}{A_{\gamma}}\int_{S_{\gamma}} J_{ij}\,\mathrm{d}S + \frac{3}{4\pi}U_j^{\gamma}\int_{S_{\gamma}} K_{ijk}\, n_k \,\mathrm{d}S \quad (\boldsymbol{x} \in S_{\gamma}), \tag{2.8b}$$

where F_j^{γ} is the total force exerted by wall patch γ on the fluid (note the change in sign between f_j and F_j^{γ}), A_{γ} is the area of the patch, U_i^{γ} is the velocity of the patch and S_{γ} indicates the surface of the path. We have dropped the $u_i^{\infty}(\boldsymbol{x})$ terms in (2.8) because, for a bounded domain, $u_i^{\infty}(\boldsymbol{x}) = 0$. Note that, because the velocity of patch

γ is prescribed, U_i^γ appears on the left-hand side of (2.8*b*) rather than $u_i(\boldsymbol{x})$ as in (2.7*b*). Equation (2.8*a*) is valid at all points that do not lie on the surface of patch γ, and is therefore applicable to sphere–patch and patch–patch interactions. Patch self-term interactions are described by (2.8*b*), which can be rewritten in a more convenient form as follows:

$$U_i^\gamma = \frac{1}{8\pi\eta}\frac{F_j^\gamma}{A^\gamma}\int_{S_\gamma} J_{ij}\,\mathrm{d}S + \frac{3}{4\pi}U_j^\gamma\int_{S_\gamma} K_{ijk}\,n_k\,\mathrm{d}S + \tfrac{1}{2}U_i^\gamma \quad (\boldsymbol{x}\in S_\gamma). \tag{2.8c}$$

In forming the interactions in $\mathscr{M}^{\mathrm{w}}$ that involve wall patches, only those terms in (2.8*a*) and (2.8*c*) that involve F_j^γ need be considered, as is apparent from the form of (2.6). The other terms can be included, with no loss of generality, in $\boldsymbol{B}$, considered in detail below. The reduction of (2.8*a*) and (2.8*c*) to the forms required for use in $\mathscr{M}^{\mathrm{W}}$ entails application of Faxén laws and integration over wall patch surfaces. The final expressions for the mobility interactions are given in Appendix A; for details see Durlofsky (1986).

2.2. *Effect of planes outside discretized region*

We now consider the effect of the far particles and plane boundaries on the motion of particles within the periodic cell for the case of a force-free suspension subject to shear through relative motion of the boundaries. Because periodic boundary conditions are applied, it might seem natural to simply discretize the x, y and y, z boundaries to the period cell and to write (2.7*b*) at each of the cell boundary elements. This procedure, though in principle correct, would introduce $6B$ additional unknowns and equations into the system, where B is the number of boundary elements in each of the periodic cell boundaries. Rather than proceed in this manner, which would clearly increase computation times considerably,we have devised an alternative method that captures the effect of the far boundaries and the suspension at very little computational cost. The key to this approach is to approximate the effect of the far plane boundaries and suspended particles on the particles in the periodic cell in an integrated (i.e. average) sense. This effect is contained in the $\boldsymbol{B}$ vector.

The $\boldsymbol{B}_U$, $\boldsymbol{B}_E$ and $\boldsymbol{B}_V$ vectors contain the contributions to the sphere and wall patch velocities from the far regions of the plane boundaries, as well as the portions of the wall patch interactions that do not involve F_j^γ. To form these vectors, we need to approximate the average force density exerted by the fluid on the walls and integrate this force density times the appropriate propagator from the edge of the periodic cell to infinity. The force density exerted by the fluid is, however, unknown; it is determined during the course of the dynamic simulation and provides the effective viscosity of the suspension. As we shall see, however, the effect of the walls outside the discretized region can still be assessed.

In the absence of particles, the force density exerted by the fluid on the upper boundary is simply $f_2^\infty = -\eta(V_2 - V_1)/H$, where V_1 and V_2 are the x-velocities of the lower and upper planes, respectively.

In systems involving finite numbers of particles, f_2^∞ is the force density exerted by the fluid on the upper boundary far from the suspended particles. Thus, for purposes of simulation, the force density of the far boundaries is known for this case. In the presence of an infinite suspension of particles, however, the force density is now given by

$$f_2 = \eta_r f_2^\infty, \tag{2.9}$$

where η_r is the relative viscosity of the suspension, defined as the ratio of the effective suspension viscosity to the pure fluid viscosity. Thus, the force density given by (2.9) is the appropriate quantity for use in (2.8*a*) and (2.8*c*) in assessing the effect of the far regions of the walls. However, the disturbance caused by an element of the wall of force density f_2 must propagate through a suspension of force- and torque-free particles, not through pure fluid. Therefore, η in (2.8) must be replaced by $\eta\eta_r$, which results in a cancellation of η_r. This indicates that the effect of the far region of the wall is the same as it would be if disturbances of force density f_2^∞ propagate through pure fluid of viscosity η.

The mathematical consequences of this conclusion are identical to those that result from considering the suspension outside the periodic cell (boundaries, fluid and suspended particles) in an averaged sense. Though the distant portion of each boundary exerts a force on the fluid, when averaged over a sufficiently large area the net force imposed by the two distant boundaries is zero (their forces are equal and opposite on average). Thus, the averaged effect of the distant portion of the suspension is an imposed shear flow, as would be expected. The forces exerted by the distant portions of the boundaries and the effective viscosity of the medium through which these disturbances propagate determine the magnitude of the imposed shear flow. The magnitude of this shear flow must, however, be consistent with the specification of the relative velocities of the two planes, the spacing between them, and the portion of the boundary that is discretized. The only shear rate that satisfies this consistency is the shear rate that corresponds to a force density on the distant boundaries of strength f_2^∞ propagating through pure fluid of viscosity η, or, analogously, a force density of strength $\eta_r f_2^\infty$ propagating through a medium of viscosity $\eta\eta_r$. Any other specification of the effects of the distant portion of the suspension results in a kinematic inconsistency in (2.6) and must therefore be rejected.

The $\boldsymbol{B}$ vectors we wish to evaluate are comprised of two contributions: (i) a kinematic contribution, resulting from the terms not involving f_j (or F_j) in (2.7) and (2.8), from both the discretized and non-discretized portions of the wall, and (ii) a dynamic contribution, resulting directly from the forcing by the non-discretized portions of the walls. Designating the first contribution $\boldsymbol{D}$ and the second contribution $\boldsymbol{B}_0$,

$$\boldsymbol{B} = \boldsymbol{D} + \boldsymbol{B}_0. \tag{2.10}$$

The $\boldsymbol{D}$ contributions are straightforward to calculate, simply entailing integrals, over all of both walls, of the kinematic terms of (2.8). The $\boldsymbol{B}_0$ vector contains integrals of the interaction functions, from the boundary of the discretized region to infinity, for both planes. The region of integration is depicted schematically in figure 1. Rather than actually integrate directly from C (the edge of the discretized region) to R, and take the limit as $R \to \infty$, we integrate from zero to R and subtract from this the integral from zero to C, in the limit $R \to \infty$; i.e.

$$f^\infty \int_C^R l_{ijk}\,\mathrm{d}S = f^\infty \int_0^R l_{ijk}\,\mathrm{d}S - f^\infty \int_0^C l_{ijk}\,\mathrm{d}S \quad \text{as } R \to \infty, \tag{2.11}$$

where l_{ijk} represents any of the interaction functions. The integrals are expressed in this way because the integrals from zero to R can be performed analytically, and the integrations of the functions from zero to C are already performed in forming $\mathcal{M}^{\mathrm{W}}$. Thus, we can express $\boldsymbol{B}_0$ as

$$\boldsymbol{B}_0 = \boldsymbol{Q} - \mathcal{M}^{\mathrm{W}} \cdot \boldsymbol{F}^\infty, \tag{2.12}$$

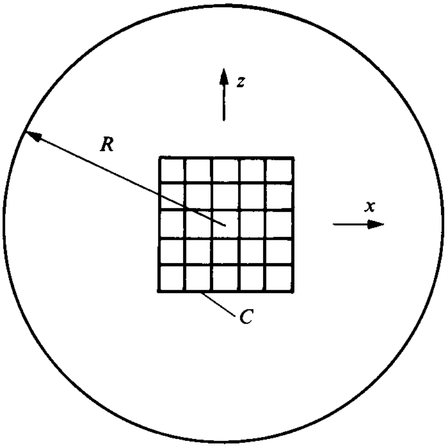

FIGURE 1. Schematic diagram depicting the region of integration from the boundary of the discretized region of the plane, denoted by C, to R, as $R \rightarrow \infty$. Rather than actually integrate from C to R, we integrate from zero to R and subtract from this the integral from zero to C.

where $\boldsymbol{Q}$ represents the vector of resultant integrations from zero to R and $\boldsymbol{F}^{\infty}$ is the force exerted by the wall patches in the absence of any particles (i.e. f^{∞} times the area of the wall patch). Combining (2.12) and (2.10) gives the final expression for $\boldsymbol{B}$. For the detailed components, see Durlofsky (1986).

In the limit $C \rightarrow 0$ (the discretized portion of the boundaries shrinks to zero) $\boldsymbol{B}$ exactly reproduces a shear flow imposed from infinity. Under these conditions, an isolated force-free sphere translates with the local fluid velocity and rotates with the local vorticity; i.e. there is no 'wall effect'. The wall effect arises because the actual force density on the boundaries, in the presence of a force-free sphere, differs from its value in the absence of the sphere, and this in turn affects the sphere velocity. This effect cannot appear in our analysis until a finite portion of the wall is discretized. When the discretized region becomes infinite ($C \rightarrow \infty$) there is no flow imposed on the system by the far region of the boundaries, and the wall effect is correctly reproduced. We note that the above discussion is applicable only to suspensions of force-free particles or finite systems of particles subject to externally imposed forces or torques. For infinite systems of particles subject to forces or torques and bounded between two infinite planes, pressure drop considerations must be taken into account. This is because the forces exerted by the boundaries are no longer necessarily equal and opposite, as is apparent from a macroscopic momentum balance. Specifically, the forces exerted by the boundaries plus the forces exerted by the particles must now balance the pressure drop through the system, and the average flow rate of the system (or equivalently pressure drop) must now be specified. Thus, because the present method is not immediately applicable to pressure driven flows, extensions are required for the simulation of infinite systems of particles subject to externally imposed forces.

The specification of the mobility problem is now complete. The mobility matrix contains far-field approximations to all the particle and near-region boundary interactions. Upon inversion, these interactions are scattered, with many-body reflections performed (see Durlofsky *et al.* for further discussion of this point), resulting in a grand resistance matrix that contains many-body interactions. The resistance matrix does not yet contain lubrication, which would only be reproduced upon inversion of $\mathscr{M}^{\mathrm{W}}$ if all moments of the sphere interactions were included and the wall were discretized infinitely finely. Lubrication can be directly introduced into the mobility invert, however, through use of exact sphere–sphere and sphere–wall solutions. We now discuss how this is accomplished.

2.3. *Adjustment for lubrication*

Upon inversion of $\mathscr{M}^{\mathrm{W}}$, the following equation set results:

$$\begin{bmatrix} F \\ S \\ T \end{bmatrix} = \begin{bmatrix} \boldsymbol{R}_{FU} & \boldsymbol{R}_{FE} & \boldsymbol{R}_{FV} \\ \boldsymbol{R}_{SU} & \boldsymbol{R}_{SE} & \boldsymbol{R}_{SV} \\ \boldsymbol{R}_{TU} & \boldsymbol{R}_{TE} & \boldsymbol{R}_{TV} \end{bmatrix} \cdot \begin{bmatrix} U \\ -E \\ V \end{bmatrix} - \begin{bmatrix} B_U \\ B_E \\ B_V \end{bmatrix}. \tag{2.13}$$

The submatrices $\boldsymbol{R}_{FU}$, $\boldsymbol{R}_{FE}$, $\boldsymbol{R}_{SU}$ and $\boldsymbol{R}_{SE}$ comprise the grand resistance matrix $\mathscr{R}$ for finite systems of particles; the grand resistance matrix here is designated $\mathscr{R}^{\mathrm{W}}$. Lubrication is introduced into $\mathscr{R}^{\mathrm{W}}$ through use of exact two-sphere resistance functions (Arp & Mason 1977; Jeffrey & Onishi 1984; Kim & Mifflin 1985) and sphere–wall resistance functions (Brenner 1961; Maude 1961; Dean & O'Neill 1963; O'Neill 1964; Goldman, Cox & Brenner 1967*a*, *b*; Cox & Brenner 1967; O'Neill & Stewartson 1967; O'Neill 1968); the matrix containing this exact two-body information is designated $\boldsymbol{R}_{2B}^{\mathrm{W}}$. Part of the two-body resistance interactions (specifically the far-field portion) is, however, already included in $(\mathscr{M}^{\mathrm{W}})^{-1}$. Thus, in order not to introduce these interactions twice, the two-body resistance interactions already contained in $(\mathscr{M}^{\mathrm{W}})^{-1}$ are subtracted from $\mathscr{R}_{2B}^{\mathrm{W}}$. The matrix composed of these two-body interactions, designated $(\mathscr{R}_{2B}^{\mathrm{W}})^{\infty}$, is formed by inverting a two-body mobility matrix containing terms to the same order in $1/r$ as $\mathscr{M}^{\mathrm{W}}$. Thus, the approximation to $\mathscr{R}^{\mathrm{W}}$, containing both near-field sphere–sphere and sphere–wall lubrication and far-field many-body effects is

$$\mathscr{R}^{\mathrm{W}} = (\mathscr{M}^{\mathrm{W}})^{-1} + \mathscr{R}_{2B}^{\mathrm{W}} - (\mathscr{R}_{2B}^{\mathrm{W}})^{\infty}. \tag{2.14}$$

The components of $\mathscr{R}_{2B}^{\mathrm{W}}$ and $(\mathscr{R}_{2B}^{\mathrm{W}})^{\infty}$ involving interactions of spheres with the boundaries require special consideration. In forming sphere–wall interactions in $\mathscr{R}_{2B}^{\mathrm{W}}$, exact sphere–wall solutions are employed when the sphere centre is within three sphere radii of the near boundary; for greater separations the $(\mathscr{M}^{\mathrm{W}})^{-1}$ interactions require no adjustment. Technically, in forming interactions involving a sphere near a wall, it is not allowable to consider either of the two planes individually. However, the results of Ganatos *et al.* (1980*a*, *b*) clearly indicate that when a sphere is within about three sphere radii of one plane and is more than about five sphere radii from the other plane, the sphere motion generally coincides with the single plane results. And further, most of the adjustments involve singular lubrication terms, whose dominant behaviour is unaffected by the presence of the far plane. Thus, use of exact sphere–wall results for our sphere–two wall system introduces only slight error and does not affect the singular behaviour at all. We note that in the singular region near the wall the elements of the resistance matrix are adjusted to recover exactly the results of Goldman *et al.* (1967*b*) for a sphere near a single plane immersed in a shear flow. As we shall see (§3), the one-sphere results of Ganatos *et al.* (1980*a*, *b*) will indeed be reproduced with good accuracy.

The near-field sphere–wall interactions introduced via $\mathscr{R}_{2B}^{\mathrm{W}}$ include the interaction of the sphere with the entire wall, not just with a particular wall patch. Thus, the interaction in $(\mathscr{R}_{2B}^{\mathrm{W}})^{\infty}$ must also account for the entire wall. This is accomplished by forming a mobility matrix, to the same order in $1/r$ as $\mathscr{M}^{\mathrm{W}}$, for the sphere and all

$\frac{1}{2}P$ wall patches comprising the near wall. Upon inversion, the $(\mathscr{R}^{\mathrm{W}}_{2B})^{\infty}$ components are combined to yield composite sphere–wall mobility invert interactions, consistent with those included in $\mathscr{R}^{\mathrm{W}}_{2B}$. This assures that no portion of the sphere–wall interaction is counted twice.

2.4. *Particle trajectories and suspension viscosity*

Setting $\boldsymbol{E}$ to zero, the equation set to solve for the sphere velocities is:

$$\boldsymbol{R}_{FU}\cdot \boldsymbol{U} = \boldsymbol{R}_{FU}\cdot \boldsymbol{B}_U + \boldsymbol{R}_{FE}\cdot \boldsymbol{B}_E - \boldsymbol{R}_{FV}\cdot(\boldsymbol{V}-\boldsymbol{B}_V) + \boldsymbol{F}, \tag{2.15}$$

where, with the velocities of the planes prescribed, the right-hand side is known. We solve (2.15) using the Cholesky method, which is applicable to symmetric, positive definite matrices. ($\boldsymbol{R}_{FU}$ is required to be positive definite due to the dissipative nature of the system.) Given $\boldsymbol{U}$, the sphere centre positions ($\boldsymbol{x}_{\mathrm{s}}$) are determined via

$$\frac{\mathrm{d}\boldsymbol{x}_{\mathrm{s}}}{\mathrm{d}t} = \boldsymbol{U}(\boldsymbol{x}_{\mathrm{s}}), \tag{2.16}$$

which can be solved using any accurate integration scheme. Once $\boldsymbol{U}$ is determined, $\boldsymbol{T}$, the forces exerted by the walls, can be computed by a matrix multiplication (no equation set need be solved):

$$\boldsymbol{T} = \boldsymbol{R}_{TU}\cdot(\boldsymbol{U}-\boldsymbol{B}_U) - \boldsymbol{R}_{TE}\cdot \boldsymbol{B}_E + \boldsymbol{R}_{TV}\cdot(\boldsymbol{V}-\boldsymbol{B}_V). \tag{2.17}$$

Given $\boldsymbol{T}$ the relative viscosity (η_{r}) of the suspension can be calculated:

$$\eta_{\mathrm{r}} = \frac{T_x H}{L_x L_z (V_2 - V_1)}, \tag{2.18}$$

where T_x is the x-component of $\boldsymbol{T}$ summed over all the wall patches of either wall ((2.18) is actually written for the upper wall; for the lower wall $(V_1 - V_2)$ replaces $(V_2 - V_1)$). Note that, in computing η_{r} through knowledge of the wall forces, the suspension viscosity is determined through macroscopically observable quantities, just as in a laboratory experiment. The y-components of $\boldsymbol{T}$ sum to give the normal forces exerted by the walls on the fluid. In all the simulation results we shall present, the normal velocities of the boundaries are prescribed to be zero. Alternatively, however, the normal forces exerted by the walls could be specified and their dilatational velocities computed. This latter specification corresponds to experimental arrangements for studies of granular flow where, at high enough concentrations of solids, the suspension cannot flow until the bounding walls dilate.

Before turning to actual simulation results, a few remarks regarding specific aspects of the numerical procedure are in order. Because significant changes in $\mathscr{M}^{\mathrm{W}}$ occur only when the relative separation of particles changes by amounts comparable to the particle size, while $\mathscr{R}^{\mathrm{W}}_{2B}$ changes on the scale of lubrication forces, which vary with the separation of particle surfaces, a multiple timescale method can be used, with $\mathscr{M}^{\mathrm{W}}$ formed and inverted relatively infrequently. This results in substantial computational savings, as the inversion of the grand mobility matrix is the most time consuming step in the numerical procedure.

In simulations of unbounded suspensions subject to an imposed bulk shear flow, the following relationship holds for all values of y:

$$u^{\infty}_x(y_\beta) = u^{\infty}_x(y_\alpha) + 2E_{xy}(y_\beta - y_\alpha), \tag{2.19}$$

where u_x^∞ designates the flow at infinity, E_{xy} the (x, y)-component of the bulk rate of strain and y_α and y_β the sphere positions in y. This relationship must hold exactly for the singularities in the sphere interaction functions to balance (specifically the $\boldsymbol{A}$ and $\boldsymbol{G}$ functions, see Kim & Mifflin 1985); otherwise excessive overlap may occur when two spheres in shear flow come into near contact. For the problem at hand, this implies that $\boldsymbol{B}_E$ must be a constant independent of position and that $\boldsymbol{B}_U$ and $\boldsymbol{B}_V$ must satisfy an equation of the form (2.19). Unfortunately, this is not quite the case; $\boldsymbol{B}_E$ varies slightly with position. Therefore, to assure that excessive particle overlap does not occur in many-particle simulations, $\boldsymbol{B}_U$, $\boldsymbol{B}_E$, and $\boldsymbol{B}_V$ are adjusted (linearized) to satisfy an equation of the form (2.19). For the simulation results presented, this entails at most a 10–15% modification to any of the $\boldsymbol{B}$ components. These adjustments to $\boldsymbol{B}$ become small as larger portions of the bounding planes are discretized at constant H. Specifically, the nonlinearities in $\boldsymbol{B}$ (which necessitate the adjustments) scale as $O(H/L_x)$ for $L_x \gg H$. Particle overlap can also occur if the integration timestep is not sufficiently small. This problem arises independent of the accuracy of the final resistance matrix; it occurs even for only two spheres, where the exact interactions are known. To avoid a prohibitively small timestep requirement, we allow some particle overlap (typically less than 10^{-5} surface overlap), though the sphere interactions are computed as though the surfaces are 10^{-8} apart, as the lubrication formulae do not allow negative surface to surface spacings. This procedure does not appear to compromise the accuracy of the method (we observed no difference in limited tests that compared the 10^{-8} surface separation specification to a 10^{-6} specification).

Let us briefly discuss the computation time requirements of the general method. The most computationally intensive step is the inversion of the grand mobility matrix, requiring $O[(11N+3P)^3]$ operations in three dimensions and $O[(6N+2P)^3]$ operations for monolayer simulations. The two alternative methods suggested at the beginning of this section would result in fewer operations for the inversion of the grand mobility matrix, but these savings might be somewhat countered by more computationally intensive function evaluations in the formation of the mobility matrix. For simulations with very large numbers of particles, however, a simulation based on the fundamental solution for a point force between two infinite planes (Liron & Mochon 1976) would almost certainly be the most computationally efficient, as the $O(N^2)$ fill problem becomes computationally inconsequential compared to the $O(N^3)$ inversion.

The specification of the simulation method is now complete. The method includes both dominant many-body effects, involving both particles and boundaries, and near-field lubrication effects. By prescribing the plane boundaries to translate relative to one another a shear flow is generated, resulting in particle motion. The suspension viscosity is determined through calculation of the boundary forces, precisely as in an actual experiment.

3. Model problem results

In order to assess the general accuracy and capabilities of the method, we now present simulation results for systems of one and six spheres confined between two plane walls. Because the sphere interactions are computed as in Durlofsky *et al.* 1987, the excellent agreement with known solutions for finite systems of spheres obtained in that paper applies in the present case as well. Therefore, we shall here emphasize test problems in which the boundaries play an important role. In these examples,

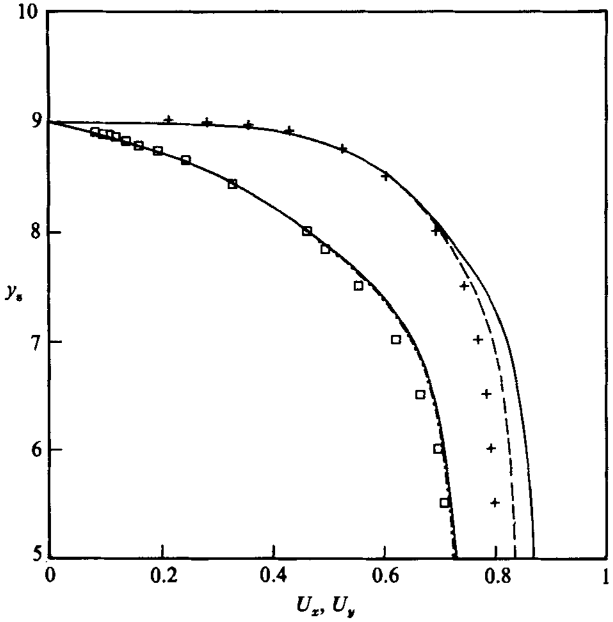

FIGURE 2. Dimensionless sphere velocities resulting from imposed forces in the x- and y-directions for a sphere between two stationary planes spaced 10 sphere radii apart. The upper and lower solid lines correspond to simulation results for U_x and U_y, respectively, with 98 wall patches and $L_x = L_z = H$, the dashed line to the simulation result for U_x with 162 wall patches and $L_x = L_z = 2H$, the broken line to the simulation result for U_y with 162 wall patches and $L_x = L_z = H$, and the + and □ to the results of Ganatos *et al.* (1980*a*, *b*) for U_x and U_y, respectively. Results are shown only for $5 \leqslant y_s < 9$ as the solutions are symmetric about $y = 5$.

periodic boundary conditions are applied in the x-direction only, though the boundaries extend to infinity in both x and z.

The first test problem considered involves a single sphere of radius a confined between two planes spaced 10 sphere radii apart ($H = 10$). From here on, all distances will be non-dimensionalized by a. Figure 2 depicts the sphere velocity in the x- and y-directions (U_x and U_y) resulting from applied forces of magnitude $6\pi\eta a$ in the x- and y-directions, respectively, as a function of y_s, the position of the sphere centre. Results are shown only for $5 \leqslant y_s < 9$, as the solutions are symmetric about the centreline $y = 5$. In the figure, the upper solid line corresponds to the simulation result for U_x with 98 wall patches (49 patches per wall) and $L_x = L_z = H$ (i.e. a cubic periodic cell), the lower solid line corresponds to the simulation result for U_y with the same boundary specifications, the dashed line corresponds to the simulation result for U_x with 162 wall patches and $L_x = L_z = 2H$, the broken line to the simulation result for U_y with 162 wall patches and $L_x = L_z = H$, and the plus signs and squares to the results of Ganatos *et al.* (1980*a*, *b*) for U_x and U_y, respectively. The agreement between the simulation results and the results of Ganatos *et al.* is clearly excellent when the sphere is near the boundary ($8 \leqslant y_s < 9$), with discrepancies apparent for $5 \leqslant y_s < 8$. The discrepancies are clearly larger for the U_x results than for the U_y results, and in both cases accuracy is improved by increasing the number of wall patches. The largest discrepancy between the results of Ganatos *et al.* and the 98 wall patch simulation results are about 9% for U_x and 5% for U_y; for the 162 wall patch simulations the discrepancies are reduced to 5% for $U_x(L_x/H = 2)$ and 4% for $U_y(L_x/H = 1)$.

Number of wall patches	L_x/H	Area of one wall patch	U_x	U_y
18	1	11.11	0.869	0.736
50	1	4.00	0.861	0.719
98	1	2.04	0.857	0.712
162	1	1.23	0.854	0.708
18	2	44.44	0.852	0.758
50	2	16.00	0.836	0.739
98	2	8.16	0.830	0.729
162	2	4.94	0.826	0.724
98	1.5	4.59	0.836	0.718
98	3	18.37	0.833	0.744
98	4	32.65	0.841	0.754
Ganatos *et al.*			0.79	0.69

TABLE 1. U_x and U_y results for a single sphere ($y_s = 6$) translating between two stationary planes spaced 10 sphere radii apart

A wider range of variation in both the number of wall patches and the $L_x/H(=L_z/H)$ ratio is displayed in table 1 for a sphere located at $y_s = 6.0$. Taking the Ganatos *et al.* results as exact, it is apparent that the U_x simulation results improve with increased number of wall patches (P) at fixed L_x/H and with increased L_x/H at fixed P for $1 \leqslant L_x/H \leqslant 2$. The U_y simulation results also improve with increased P at fixed L_x/H, but worsen with increased L_x/H at fixed P. The key to understanding these behaviours is consideration of the study of Liron & Mochon (1976) of the fundamental solution for Stokes' flow between two parallel plane walls. Liron & Mochon found that velocity disturbances caused by motion normal to the boundaries decay exponentially with distance, while velocity components in directions parallel to the plane walls caused by motion parallel to the boundaries decay only as $1/r^2$, where r is the distance from the disturbance. Due to the relatively slow decay of parallel disturbances, the U_x results improve as larger areas of the plane are discretized, even though the individual wall patches become larger. The rapid decay of disturbances normal to the boundaries, however, render the U_y results more sensitive to the level of discretization (i.e. wall patch size) than to the total area of discretized wall; consequently these results do not improve as larger areas of wall are discretized at the expense of wall patch size.

We note that, even with very large areas of the boundaries discretized very finely, the exact results for a sphere between two walls might not be recovered unless higher moments were included in the sphere interactions. This does not appear to be necessary, however, in light of the only slight discrepancies apparent at this level of approximation. We note further that the simulation results for U_x and U_y displayed in figure 2 extend all the way to sphere–wall contact. Because both velocities tend to zero as the sphere approaches the wall, there does not appear to be any dramatic effect in this limit. However, were we to plot the forces required to translate the sphere at constant velocity, these results would be seen to diverge as $\ln \epsilon$ for parallel motion, where ϵ is the spacing between the sphere and wall surfaces, and as $1/\epsilon$ for normal motion. Because we introduce lubrication analytically into the resistance matrix, the simulation method has no difficulty reproducing this singular behaviour. An approach such as that of Ganatos *et al.*, however, requires an increasing number of collocation points to resolve singularities in the limit $\epsilon \rightarrow 0$, resulting in great computational expense.

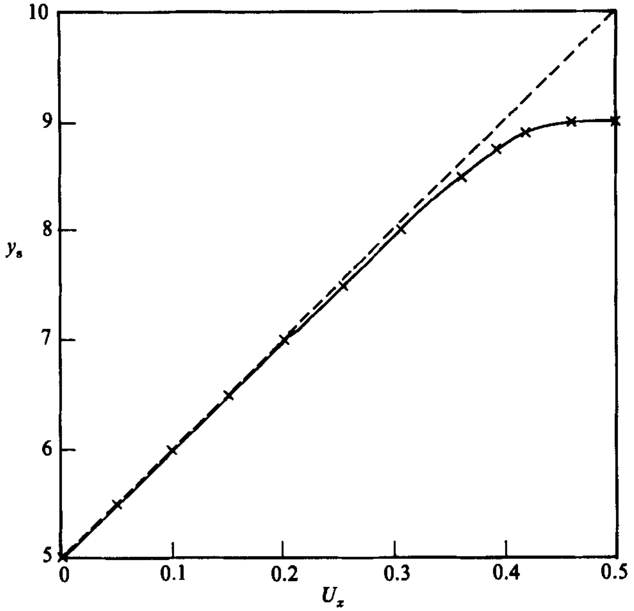

FIGURE 3. Dimensionless translational velocity of a single force- and torque-free sphere immersed between two planes spaced 10 sphere radii apart, with the lower plane translating at $V_1 = -0.5$ and the upper plane at $V_2 = 0.5$. The solid line corresponds to the simulation result with 98 wall patches and $L_x = L_z = H$, × to the results of Ganatos *et al.* (1982) and the dashed line to the velocity profile of pure fluid in the absence of the sphere.

Figure 3 depicts the translational velocity of a single force- and torque-free sphere immersed between two planes spaced 10 sphere radii apart. The upper plane translates at $V_2 = 0.5$ and the lower plane at $V_1 = -0.5$. The solid line is the simulation result with $P = 98$ and $L_x/H = 1$, the × values are the results of Ganatos *et al.* (1982) and the dashed line is the velocity profile for pure fluid. The agreement is clearly very good over all values of y_s.

Although the walls are treated individually in adjusting the sphere–wall resistance interactions, the agreement between our results and those of Ganatos *et al.*, evident in figures 2 and 3, persists even for plane–plane spacings of as few as 2.5 sphere radii. At such near spacings, the individual treatment of the walls might be expected to introduce some error. However, at near spacings, the singularities in the sphere–plane interactions dominate, and these are handled accurately.

We now turn to a model problem that more clearly displays the importance of correctly modelling sphere–sphere and sphere–wall lubrication in the resistance matrix. The initial configuration is shown in figure 4. Six spheres are oriented in a line at an angle of 135° to the x-axis. The dimensionless spacing between each pair of sphere surfaces ϵ is 10^{-4} and the spacing between the spheres adjacent to the planes and the plane is also 10^{-4}. The lower plane is stationary and the upper plane translates at $V_2 = 1$; for this run $P = 50$ and $L_x/H = 1$. The initial sphere velocities are shown in table 2 (Ω_z is the angular velocity in the z-direction), with the sphere numbering corresponding to that in figure 4. Note that the translational velocities are antisymmetric about the midline $y = \frac{1}{2}H$ and the angular velocities symmetric. Especially interesting are the actual values of the x-velocities – the spheres translate in x almost as a plug, with all six spheres moving with the average velocity of the two planes (0.5) to within about 10%. This plug-flow like behaviour is captured through

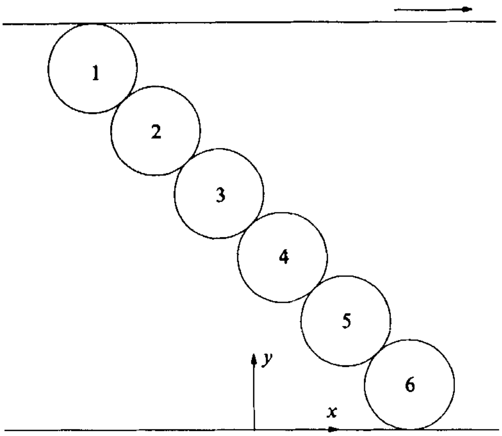

FIGURE 4. Initial configuration for the six-sphere simulation. The spacing between adjacent sphere surfaces and between the surfaces of the spheres nearest the plane and the plane is 10^{-4} sphere radii. The spheres are oriented along the compressional axis; the upper plane translates in the positive x-direction and the lower plane is stationary.

Sphere number	U_x	U_y	Ω_z
1	0.5057	0.0002789	−0.07048
2	0.5383	0.03498	0.01636
3	0.5230	0.02188	−0.02359
4	0.4770	−0.02188	−0.02359
5	0.4617	−0.03498	0.01636
6	0.4943	−0.0002789	−0.07048

TABLE 2. Initial velocities for six sphere chain

correctly modelling the lubrication interactions between spheres and between spheres and the boundaries. This simple example may qualitatively describe suspension behaviour in concentrated systems, where plug-like flow is observed experimentally under some conditions.

Figure 5 depicts the time evolution of the six sphere configuration. By $t \approx 20$ (time is non-dimensionalized by a/V_2) the spheres achieve a linear configuration that appears to be a mirror image of the initial configuration, though this is not the case, as can be demonstrated by reversibility arguments as follows. Were a configuration a mirror image of the initial configuration then, by reversibility, an intermediate arrangement appearing midway in time between the initial and mirror-image configurations would have to itself possess reflectional symmetry about a line $x =$ constant. The only configurations that could exhibit such a symmetry correspond to either particles arranged vertically on the line $x =$ constant, which is not geometrically possible in the present arrangement, or to two sets of three particles (or three sets of two) arranged symmetrically about $x =$ constant, which entails a rupture and a reformation of the six particle configuration that is clearly not observed. Thus the $t \approx 20$ configuration is not a mirror image of the initial arrangement. By $t = 25$ the chain has rotated away from the two planes and has ruptured into three groups of two spheres.

Although the six sphere configuration does not reform a mirror image of the initial configuration, it does indeed obey reversibility. Upon reversal of the direction of

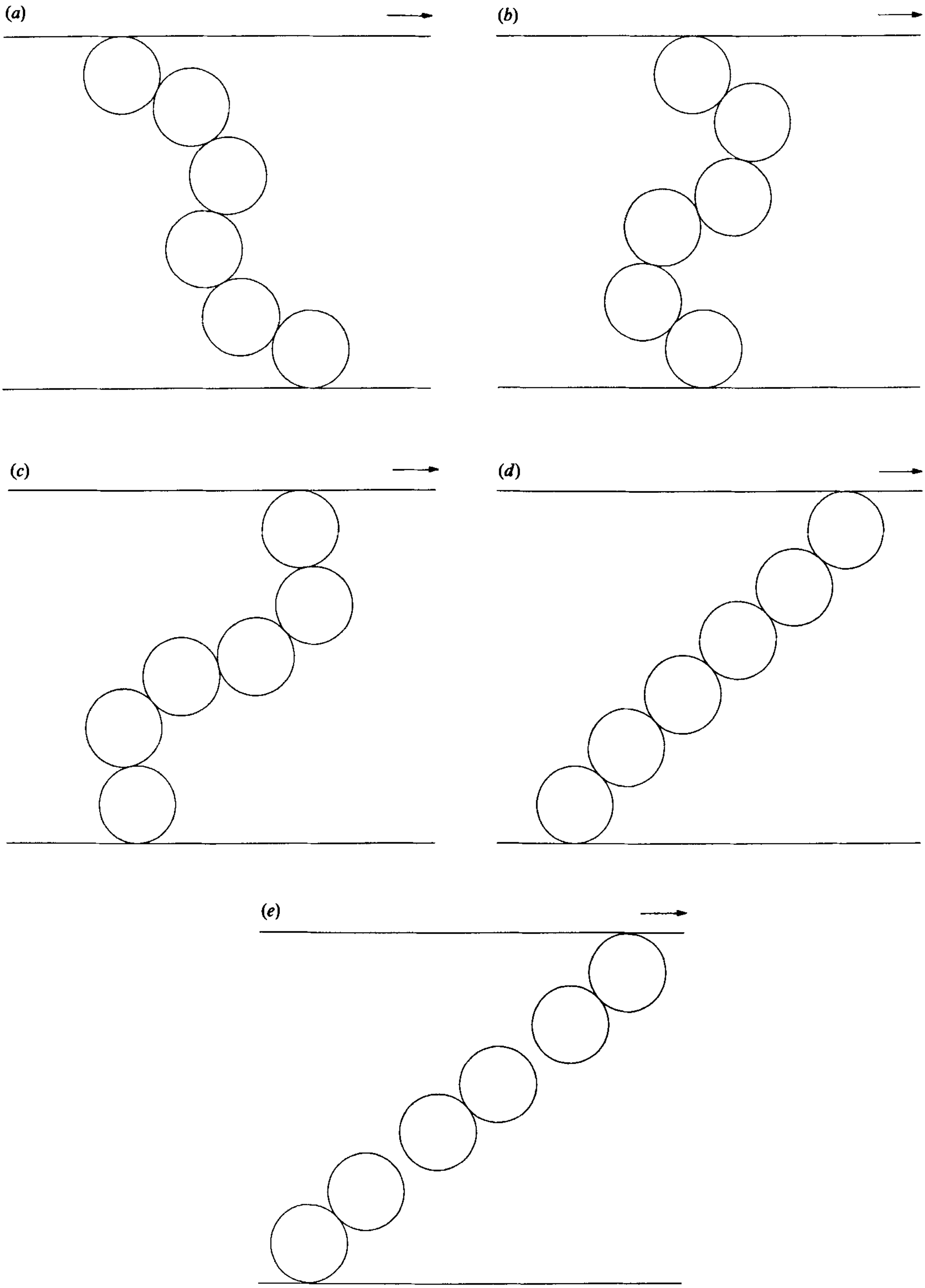

FIGURE 5. Time evolution of the six-sphere configuration. (*a*) $t = 5$, (*b*) $t = 10$, (*c*) $t = 15$, (*d*) $t = 20$ and (*e*) $t = 25$. The configuration at $t = 20$ is not a mirror image of the initial configuration (see text).

translation of the upper plane, the spheres retrace their original path with extremely good accuracy. For example, in a simulation where the direction of translation of the upper plane was reversed at $t = 18$, the x-positions of the spheres at $t = 23$ agree with those at $t = 13$ to three decimal places; the magnitudes of the velocities show comparable agreement. This agreement persists all the way to $t = 36$, where the initial condition is reproduced. It must be emphasized, however, that in general, owing to the chaotic nature of the many particle system, complicated sphere configurations will not display reversibility over long times. This is apparent from the evolution equation (2.16), a set of $6N$ coupled, nonlinear ordinary differential equations, which can, in general, yield chaotic solutions.

The general simulation method has now been shown to be capable of both accurately modelling the motion of a single sphere confined between two plane boundaries and of following the time evolution of a configuration of strongly interacting spheres in motions fundamentally affected by the presence of plane boundaries. We now proceed with simulations of many-particle suspensions.

4. Monolayer suspension simulations

In this section we shall present dynamic simulation results for sheared suspensions of spheres confined to a monolayer, i.e. the sphere centres are all prescribed to lie in a single plane oriented perpendicular to the plane boundaries. Monolayer simulations are considerably less computationally intensive than full three-dimensional simulations (each sphere now has only six unknowns associated with it, specifically two unknown forces, one torque and three independent stresslet components, as opposed to 11 in three dimensions, and each wall patch now has two unknown force components, as opposed to three for three-dimensional simulations), while, as we shall see, generally retaining the essential physics of three-dimensional systems. The measure of particle density in monolayer systems is areal fraction ϕ_A, rather than volume fraction in three dimensions, defined as

$$\phi_A = \frac{N\pi a^2}{HL_x}. \tag{4.1}$$

In monolayer simulations, periodic boundary conditions are only imposed in the x-direction (direction of flow), though the boundaries extend to infinity in both x and z.

The first sheared suspension simulation demonstrates viscous resuspension, a phenomenon observed experimentally by Gadala-Maria (1979) and Leighton & Acrivos (1986). These investigators found that an initially settled arrangement of identical non-Brownian spheres resuspended when subjected to shear, under conditions of particle Reynolds number as low as 10^{-6}. The pertinent parameter in these problems is a Shields parameter, which provides the ratio of viscous to gravitational forces. Experimental results indicate that the increase in the bed height is proportional to the Shields parameter. The theoretical analysis of Leighton & Acrivos, which assumes that viscous resuspension derives from a competition between gravitational forces and shear-induced diffusion, arrives at the same conclusion.

Leighton & Acrivos (1987) suggest that three-body interactions may contribute to shear-induced particle migrations. Along these lines, Hassonjee, Pfeffer & Ganatos (private communication) present calculations for three spheres in a shear flow in which the spheres interact in such a way as to induce upward motion. Their calculations involve, however, one free and two fixed spheres, so the connection between their results and the viscous resuspension of force-free spheres is not entirely clear. Leighton & Acrivos (1987) emphasize, however, that non-hydrodynamic interparticle interactions, such as irreversible surface contact due to surface roughness, will act to destroy the reversibility of the hydrodynamic interactions, leading to particle drift. Though such effects are undoubtedly present in concentrated suspensions, we refrain from identifying any particular effect as solely responsible for viscous resuspension. Instead, we note the chaotic nature of (2.16), which allows for irreversibility, and thus particle drift, in a system of particles that interact purely hydrodynamically.

Shown in figure 6(*a*) is the initial configuration for our viscous resuspension simulation. The horizontal lines represent the plane boundaries and the vertical lines the edges of the periodic cell; note that the configuration is periodically replicated in the x-direction. To obtain this configuration, the particles were first arranged hexagonally, with a very small (0.05) surface to surface spacing, and then perturbed randomly. The configuration is therefore not necessarily that which would result from sedimentation, but should be representative of an actual sediment layer. One interesting and important feature to note is that in simulations in which the spheres were not perturbed from the perfect hexagonal arrangement, the layers simply slipped relative to one another, periodically reforming the initial configuration. Therefore, no resuspension occurred. Once the symmetry of the initial configuration is broken, however, the particles resuspend. This sensitivity to the initial configuration is a hallmark of the chaotic nature of the particle evolution equations.

In the present simulation, short-ranged repulsive forces, intended to qualitatively model sphere roughness, were included in the sphere–sphere interactions. These forces are of the form

$$\boldsymbol{F}_{\alpha\beta} = F_0 \frac{\tau \mathrm{e}^{-\tau\epsilon}}{1-\mathrm{e}^{-\tau\epsilon}} \boldsymbol{e}_{\alpha\beta}, \tag{4.2}$$

where $\boldsymbol{F}_{\alpha\beta}$ is the force exerted on sphere α by sphere β, F_0 is the force magnitude, τ is related to its range, ϵ is the spacing between the surfaces of spheres α and β and $\boldsymbol{e}_{\alpha\beta}$ is the unit vector connecting the sphere centres. In the simulation, $\tau = 1000$ and $F_0 = 0.001$, giving a repulsive force of magnitude unity for $\epsilon \approx 0.0024$. Simulations performed without any interparticle forces did display viscous resuspension, though the spheres tended to form large clusters which only slowly rearranged, resulting in slow resuspension. The introduction of short-ranged interparticle forces accelerates the resuspension process as it destroys tightly packed clusters.

The sequence of figures 6(*b*)–6(*e*) display the resuspension process. In this simulation, the upper plane translates with velocity $V_2 = 0.5$ and the lower plane with velocity $V_1 = -0.5$; 27 spheres are included in the simulation with $H = 18.45$. No gravitational forces are imposed on the spheres, giving a Shields parameter of infinity. Time (t) is non-dimensionalized by $a/(V_2 - V_1)$. Initially, the sphere centre farthest from the lower plane ($y = 0$) is located at $y = 4.65$; by $t = 500$ (figure 6(*b*)) the farthest sphere is located at $y = 8.93$, at $t = 1000$ (figure 6(*c*)), $y = 11.96$; at $t = 1500$ (figure 6(*d*)), $y = 13.28$, and at $t = 2000$ (figure 6(*e*)), $y = 14.57$. Clearly the particles resuspend, with the bed height (defined here as the location of the sphere farthest from the lower plane) steadily increasing with time. Because the Shields parameter is infinite, the experimental findings of Leighton & Acrivos suggest that the particles would ultimately resuspend all the way to the upper plane. Our

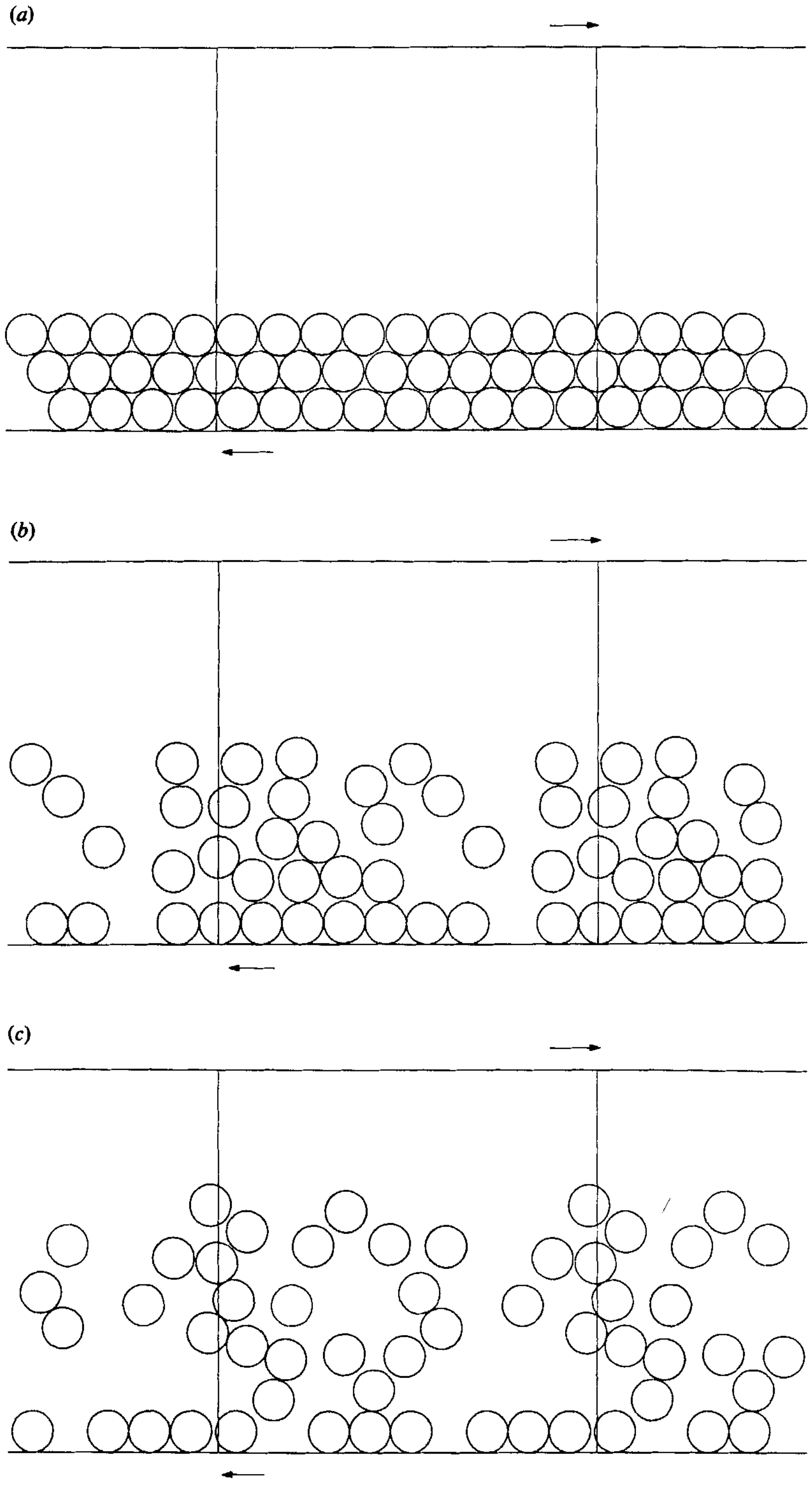

FIGURE 6(*a–c*). For caption see facing page.

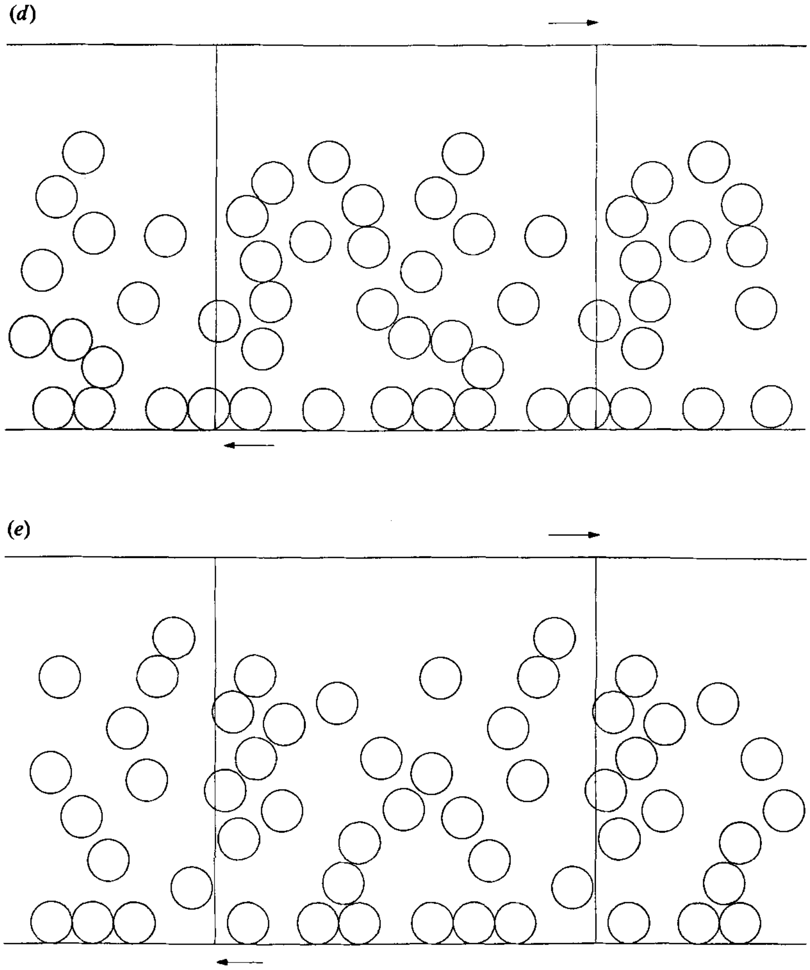

Figure 6. Simulation of the viscous resuspension of a monolayer of neutrally buoyant spheres. The lower plane translates at $V_1 = -0.5$ and the upper plane at $V_2 = 0.5$. The initial configuration (*a*) is a randomized hexagonal arrangement, in (*b*) $t = 500$, (*c*) $t = 1000$, (*d*) $t = 1500$ and (*e*) $t = 2000$. The bed height increases with time, though at a decreasing rate.

simulation results also suggest this, though they indicate that the rate of increase of the bed height decreases with time, and therefore the simulation might require considerably more time to achieve full resuspension.

One of the great advantages of dynamic simulation is that the suspension microstructure is known at every instant in time, allowing macroscale properties to be understood in terms of the microstructure. In the problem at hand, the macroscale quantity of interest is the bed height. From the simulation results, we can explain the relationship between the increase in bed height with time and the microstructure as follows. Particles initially form clusters, which rotate *en masse* with the shear flow and are eventually broken apart, releasing particles into regions of low particle concentration. These 'free' particles then interact with the clustered particles, freeing more particles from the clusters and causing a continual decrease in the size of the larger clusters. This results in particle motion toward the upper plane (resuspension). As the clusters decrease in size the resuspension process slows, as is

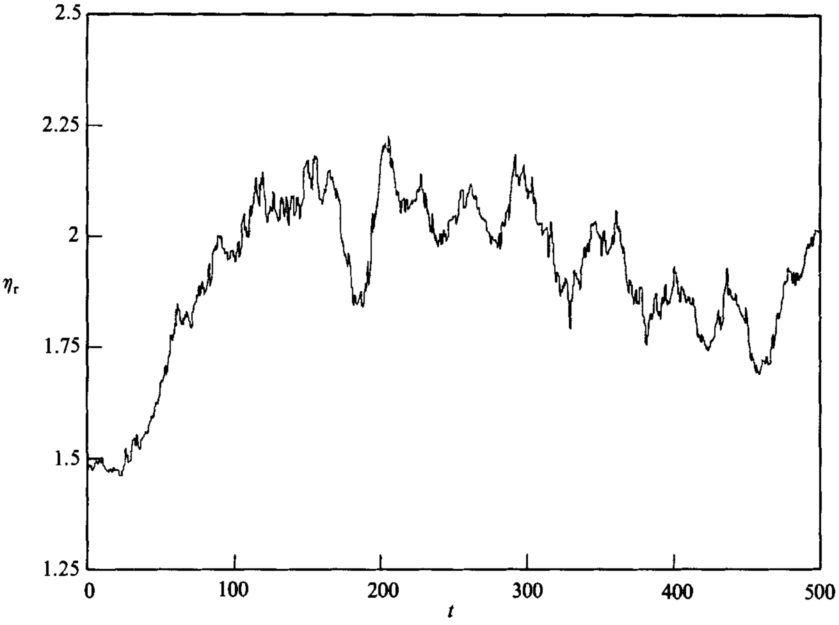

FIGURE 7. Variation of relative viscosity η_r with time for a monolayer simulation of 49 spheres at $\phi_A = 0.3$.

apparent from the sequence of figures 6(*a–e*). Also apparent from the figures is the observation that particles initially adjacent to the plane tend to remain there, i.e. few of them resuspend. Thus, if quantitative resuspension results are desired, enough layers of particles must be included in the simulation so resuspension can be observed without normal motion of the bottom layer of particles.

We now turn to simulation results for a sheared suspension of areal fraction 0.3. In this simulation, 49 particles are included ($H = 22.65$) with no interparticle or externally imposed forces acting. The upper plane again translates at $V_2 = 0.5$ and the lower plane at $V_1 = -0.5$. The initial configuration is obtained via a hard-disk Monte Carlo simulation; it is therefore spatially homogeneous (except near the walls), unlike the initial configuration in the viscous resuspension simulation. This run proceeds until a dimensionless time of 500. Our objective here is to calculate both transient and time-average suspension quantities.

Figure 7 depicts the variation of the relative viscosity (η_r) with time for the $\phi_A = 0.3$ simulation. In computing η_r for a monolayer system, (2.18) requires slight modification; see Durlofsky (1986) for details. Initially ($t < \sim 100$), the simulation results indicate that η_r increases with time, but by $t \approx 100$ the relative suspension viscosity no longer shows a definite trend, though short-time fluctuations are clearly apparent. Such fluctuations are not uncommon to monolayer systems. Experimental investigations of sheared monolayer suspensions, performed by Bouillot *et al.* (1982) and Blanc *et al.* (1983), also report large fluctuations in relative viscosity, with the magnitude of the fluctuations increasing with decreasing system size.

Figure 8 depicts the instantaneous suspension microstructure at two times: (*a*) $t = 188.1$, where $\eta_r = 1.84$ and (*b*) $t = 206.1$, where $\eta_r = 2.23$. These two times correspond to relative extremes in η_r, though the variation in η_r is not that large between the two times. Most striking about the microstructures in figure 8 are the relatively large clusters of nearly touching spheres, some containing as many as eight

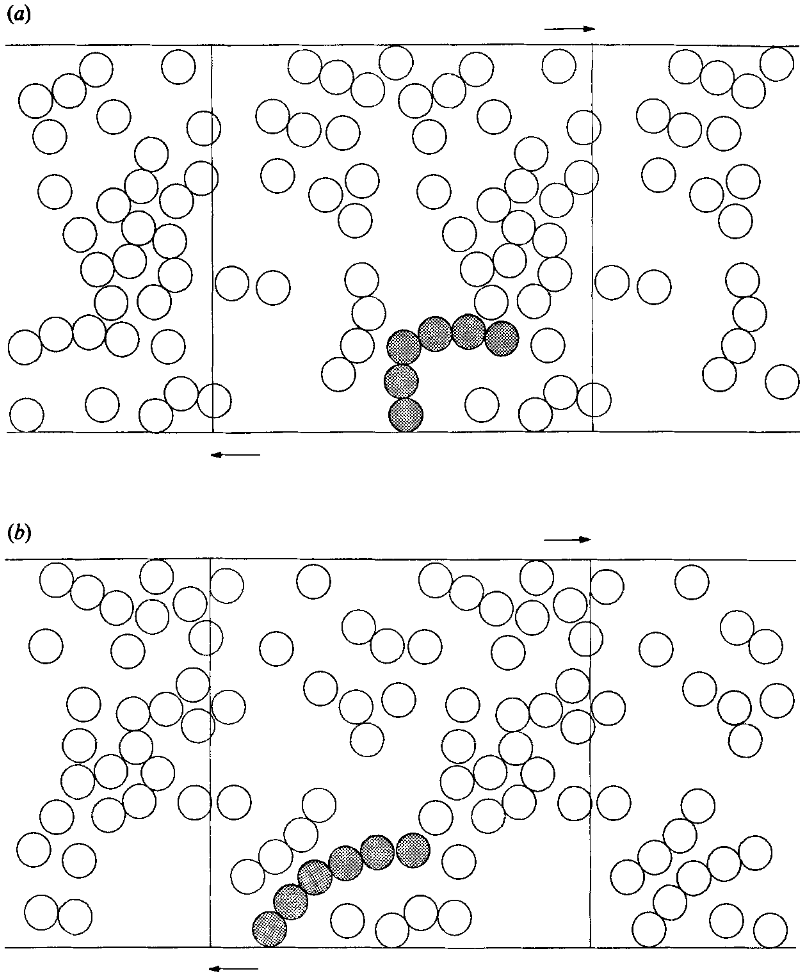

FIGURE 8. Instantaneous suspension microstructure for the $\phi_A = 0.3$ simulation at (*a*) $t = 188.1$ and (*b*) $t = 206.1$. Note the *en masse* rotation of the shaded cluster with the shear flow.

or nine particles. Also of interest is the dynamics of these clusters; the *en masse* rotation of the shaded cluster with the shear flow is evident in figure 8, as is the rotation of the smaller cluster of four spheres to its left. In fact, the difference in relative viscosity between the two configurations may be explained qualitatively in terms of the orientation of the clusters. Specifically, clusters aligned along the extensional axis of the shear flow result in larger viscosities than identical clusters not so aligned. From figure 8 it appears that the larger clusters are more closely aligned with the extension at the later time, which corresponds to the higher η_r.

Until now we have only considered instantaneous suspension properties. We now turn to a discussion of some time-average results. These results represent averages over the period $100 \leqslant t \leqslant 500$; the transient period $0 < t < 100$ is not included. Figure 9 depicts the time average sphere centre density profile. The sphere centre density, ρ_S, is calculated by dividing the domain into a number of slices in y (in this case 50) adding up the total number of sphere centres in each slice over the period $100 \leqslant t \leqslant 500$ and dividing by the number of sphere centres that would lie in the slice if the sphere centres were homogeneously distributed. Apparent in figure 9 are wall

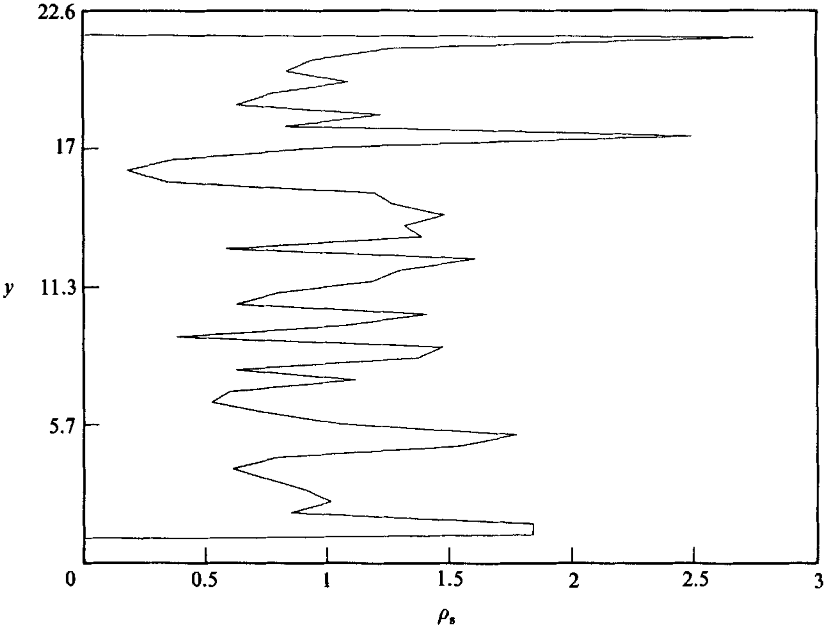

FIGURE 9. Time average sphere centre density profile for the $\phi_A = 0.3$ simulation. Note the wall exclusion areas followed by large peaks in sphere density.

exclusion areas followed by large peaks in density near the two boundaries. The density exhibits large fluctuations in the core rather than a more or less constant ρ_s of about unity, as might be expected. A uniform density might be recovered if the simulation were continued out to longer times. Despite the fluctuations in ρ_s, the particle average x-velocity profile shown in figure 10 shows very little fluctuation. The solid line represents the average particle velocity and the dashed line the velocity profile of pure fluid in the absence of particles. The two curves clearly coincide, indicating that at $\phi_A = 0.3$ the spheres translate on average nearly as pure fluid. Displayed in figure 11 is the mean-square sphere y-velocity profile, $\langle U_y^2 \rangle$, which gives an idea of the magnitudes of the sphere y-velocities and is also closely related to particle dispersion. Clearly $\langle U_y^2 \rangle$ approaches zero at both boundaries and is nearly constant in the core with the exception of the large peak at $y = 16.1$. This value of y, however, corresponds to an extremely low $\rho_s (\rho_s = 0.18)$, so the peak in $\langle U_y^2 \rangle$ is probably not statistically significant.

Some of the time average simulation results can be compared to the experimental findings of Bouillot *et al.* and Blanc *et al.* However, it must be noted that the velocity fields in the absence of particles in the experiments were not linear, so all comparisons are at best qualitative. For $\phi_A = 0.3$, the experiments give $\eta_r = 1.64$; the $100 \leqslant t \leqslant 500$ average simulation η_r is 1.97. The simulation viscosity results would be expected to exceed the experimental findings because, experimentally, particles are not constrained to lie in the monolayer while numerically they are, which assures that stresses are transmitted from sphere to sphere more efficiently in simulation than experimentally. The experimental results also indicate that the particle average streamwise velocity profile ($\langle U_x \rangle$) coincides with the pure fluid velocity profile for $\phi_A < 0.4$, in agreement with our findings.

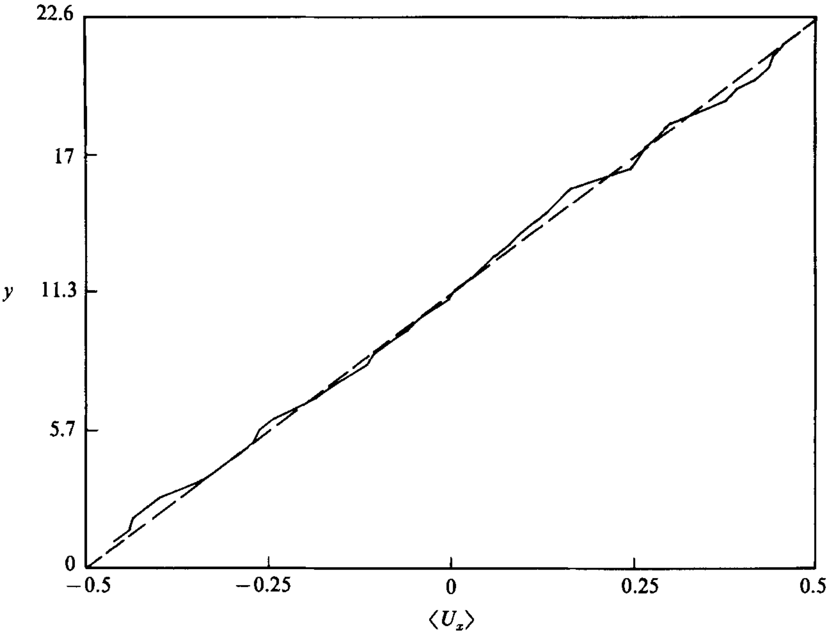

FIGURE 10. Time average particle x-velocity profile for the $\phi_A = 0.3$ simulation. The solid line represents the average particle velocity and the dashed line the velocity of pure fluid in the absence of particles.

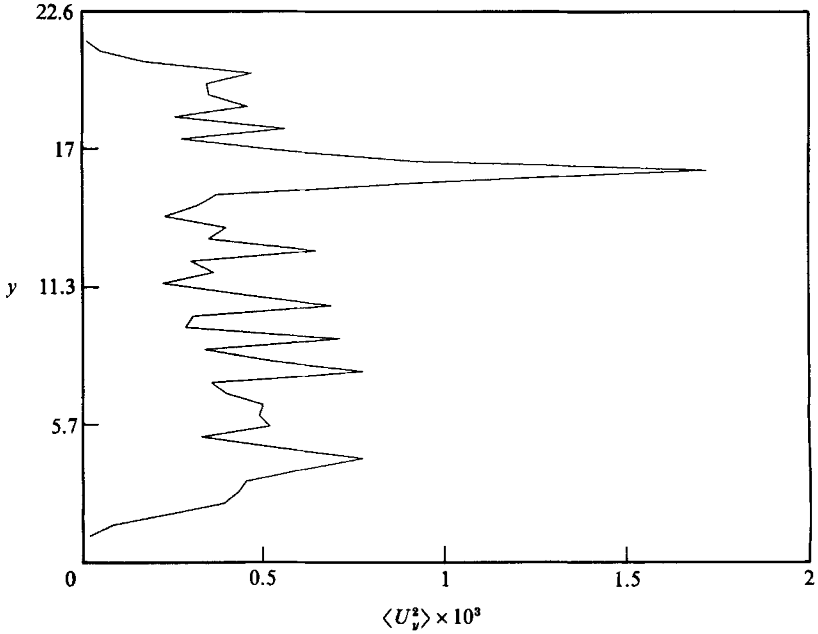

FIGURE 11. Time average mean-square sphere y-velocity profile for the $\phi_A = 0.3$ simulation. This quantity is closely related to particle dispersion.

5. Conclusions

In this paper we have developed and demonstrated a method capable of simulating the dynamic behaviour of bounded suspensions. In the formulation we have only considered systems of identical spheres, but extensions to include polydispersity, as well as non-spherical particles, are relatively straightforward. Similarly, using the approach of Bossis & Brady (1987), Brownian motion can also be incorporated into the method.

In all of our development we have addressed the two-plane problem, but it should be obvious that one-plane problems are a subset of the general method. Thus, a study involving, for example, spheres immersed in a shear flow near a single plane boundary could easily be handled with our method. For such problems, however, the fundamental solution for a point force near a single plane boundary might be an appropriate starting point; this would eliminate the need for discretization of the wall. The general method could also be adapted to study suspensions immersed in a pressure driven flow between two walls or through a tube or to suspensions subject to externally imposed forces or torques. For these problems, a macroscopic momentum balance would be required to relate the forces (if any) exerted by the particles, the forces exerted by the boundaries and the imposed pressure gradient.

The monolayer suspension simulations presented in §4 demonstrate the importance of particle clustering in the evolution of the suspension microstructure. In a subsequent paper we shall present a more comprehensive study of sheared suspension behaviour (some results are presented in Durlofsky 1986) where it will be seen that particle clustering has a profound qualitative effect on macroscale quantities such as relative viscosity in moderately concentrated systems ($\phi_A > \sim 0.35$). Indeed, we shall show that the high ϕ_A macroscale behaviour of bounded monolayer suspensions subject to shear is dominated on the microscale by the formation, rearrangement and breakup of particle clusters that span from one boundary to the other. This percolation-like behaviour indicates that above some critical ϕ_A (or critical ϕ in three dimensions) the behaviour of the suspension is fundamentally system-size dependent, and therefore boundary dominated. Specifically, in bounded monolayer suspensions subject to shear, for $\phi_A > \sim 0.35$, large fluctuations in the viscosity time trace will be evident. It will be shown that it is the formation of particle clusters that span from one boundary to the other, which effectively transmit large stresses, that results in the peaks in viscosity, and the rearrangement and breakup of these spanning clusters that produce the large viscosity fluctuations. At higher concentrations ($\phi_A = 0.6$), very large, compact clusters form, resulting in extremely high suspension viscosities as well as plug-flow-like behaviour, where all particles translate with nearly the average velocity of the two planes. These and other interesting behaviours will serve to demonstrate the qualitative importance of boundaries in concentrated suspensions subject to shear.

We wish to thank A. Heil and J. Shiang for their help with some of the simulations. Computer time was provided on the San Diego Supercomputer Center Cray X-MP through a National Science Foundation allocation. Partial support for this work was through CBT-8696067.

Appendix A. Elements of the grand mobility matrix

The grand mobility matrix $\mathscr{M}^{\mathrm{W}}$ is formed in a pairwise manner and includes sphere–sphere, sphere–wall patch and wall patch–wall patch interactions. The sphere–sphere interaction components (submatrices $\boldsymbol{M}_{UF}$, $\boldsymbol{M}_{US}$, $\boldsymbol{M}_{EF}$ and $\boldsymbol{M}_{ES}$ in (2.6)) are given in Durlofsky *et al.*; here we shall consider the others.

The submatrices $\boldsymbol{M}_{UT}$ and $\boldsymbol{M}_{ET}$ (and therefore $\boldsymbol{M}_{VF}$ and $\boldsymbol{M}_{VS}$ by symmetry) derive from pairwise sphere–wall patch interaction matrices. The one sphere–one wall patch mobility matrix is represented as follows:

$$\begin{bmatrix} \boldsymbol{U}_\alpha \\ \boldsymbol{\Omega}_\alpha \\ -\boldsymbol{E} \\ \boldsymbol{V}_\gamma \end{bmatrix} = \begin{bmatrix} \boldsymbol{a}_{\alpha\alpha} & \tilde{\boldsymbol{b}}_{\alpha\alpha} & \tilde{\boldsymbol{g}}_{\alpha\alpha} & \boldsymbol{a}_{\alpha\gamma} \\ \boldsymbol{b}_{\alpha\alpha} & \boldsymbol{c}_{\alpha\alpha} & \tilde{\boldsymbol{h}}_{\alpha\alpha} & \boldsymbol{b}_{\alpha\gamma} \\ \boldsymbol{g}_{\alpha\alpha} & \boldsymbol{h}_{\alpha\alpha} & \boldsymbol{m}_{\alpha\alpha} & \boldsymbol{g}_{\alpha\gamma} \\ \boldsymbol{a}_{\gamma\alpha} & \tilde{\boldsymbol{b}}_{\gamma\alpha} & \tilde{\boldsymbol{g}}_{\gamma\alpha} & \boldsymbol{a}_{\gamma\gamma} \end{bmatrix} \cdot \begin{bmatrix} \boldsymbol{F}_\alpha \\ \boldsymbol{L}_\alpha \\ \boldsymbol{S}_\alpha \\ \boldsymbol{T}_\gamma \end{bmatrix}, \tag{A 1}$$

where the subscript α refers to the sphere and γ to the wall patch, $\boldsymbol{F}_\alpha$ represents the force and $\boldsymbol{L}_\alpha$ the torque exerted by the sphere on the fluid, $\boldsymbol{U}_\alpha$ is the sphere translational velocity and $\boldsymbol{\Omega}_\alpha$ the rotational velocity, and all other symbols are as defined in §2.1. The notation in (A 1) is analogous to that of Jeffrey & Onishi (1984) and Kim & Mifflin (1985), and the symmetry properties discussed in those references apply here as well. The sphere self-term interactions (i.e. those components of (A 1) with $\alpha\alpha$ subscripts) are given in Durlofsky *et al.* and will not be repeated here. The wall-patch self-term $\boldsymbol{a}_{\gamma\gamma}$ will be discussed below in the context of wall patch–wall patch interactions.

Applying Faxén laws to (2.8*a*) enables us to form $\boldsymbol{a}_{\alpha\gamma}$, $\boldsymbol{b}_{\alpha\gamma}$ and $\boldsymbol{g}_{\alpha\gamma}$ directly (and therefore $\boldsymbol{a}_{\gamma\alpha}$, $\tilde{\boldsymbol{b}}_{\gamma\alpha}$ and $\tilde{\boldsymbol{g}}_{\gamma\alpha}$). Non-dimensionalizing all lengths by the sphere radii a, $\boldsymbol{a}$ matrices by $6\pi\eta a$, $\boldsymbol{b}$ by $6\pi\eta a^2$ and $\boldsymbol{g}$ by $6\pi\eta a^3$ we have the following:

$$a_{ij}^{\alpha\gamma} = \frac{3}{4}\frac{1}{A_\gamma}\int_{S_\gamma}\left\{\frac{1}{r}(\delta_{ij}+e_i e_j)+\frac{1}{3}\frac{1}{r^3}(\delta_{ij}-3e_i e_j)\right\}\mathrm{d}S, \tag{A 2}$$

$$b_{ij}^{\alpha\gamma} = \frac{3}{4}\frac{1}{A_\gamma}\int_{S_\gamma} -\frac{1}{r^2}\epsilon_{ijk}\, e_k\,\mathrm{d}S, \tag{A 3}$$

$$g_{ijk}^{\alpha\gamma} = \frac{9}{4}\frac{1}{A_\gamma}\int_{S_\gamma}\left\{\frac{1}{r^2}(e_i e_j e_k-\tfrac{1}{3}\delta_{ij}\, e_k)+\frac{1}{5}\frac{1}{r^4}(e_i\,\delta_{jk}+e_j\,\delta_{ik}+e_k\,\delta_{ij}-5e_i\, e_j\, e_k)\right\}\mathrm{d}S, \tag{A 4}$$

where $e_i = r_i/r$ and all other symbols are as defined in §2.1.

Proceeding analogously for the wall patch–wall patch interactions ($\boldsymbol{M}_{VT}$), we form pairwise patch–patch mobility matrices; i.e.,

$$\begin{bmatrix} \boldsymbol{V}_\gamma \\ \boldsymbol{V}_\delta \end{bmatrix} = \begin{bmatrix} \boldsymbol{a}_{\gamma\gamma} & \boldsymbol{a}_{\gamma\delta} \\ \boldsymbol{a}_{\delta\gamma} & \boldsymbol{a}_{\gamma\gamma} \end{bmatrix}\begin{bmatrix} \boldsymbol{T}_\gamma \\ \boldsymbol{T}_\delta \end{bmatrix}, \tag{A 5}$$

where γ and δ refer to two distinct wall patches. Assuming that the wall patches are square of half-side L_p, we have, for the patch self-term,

$$a_{ij}^{\gamma\gamma} = \frac{3}{16}\frac{1}{L_p^2}\int_{-L_p}^{L_p}\mathrm{d}x\int_{-L_p}^{L_p}\frac{1}{r}(\delta_{ij}+e_i e_j)\,\mathrm{d}z, \tag{A 6}$$

which can be evaluated to give

$$a_{xx}^{\gamma\gamma} = a_{zz}^{\gamma\gamma} = 1.9831/L_p, \quad a_{yy}^{\gamma\gamma} = 1.3221/L_p, \tag{A 7}$$

with all other components zero. For the patch–patch terms,

$$a_{ij}^{\gamma\delta} = \frac{3}{4}\frac{1}{A_{\gamma}}\left[\int_{S_{\delta}}\frac{1}{r}(\delta_{ij}+e_i e_j)\,\mathrm{d}S + \int_{S_{\gamma}}\frac{1}{r}(\delta_{ij}+e_i e_j)\,\mathrm{d}S\right] - \frac{3}{4}\frac{1}{r}(\delta_{ij}+e_i e_j). \qquad \text{(A 8)}$$

where the first integral is evaluated from the centre of wall patch γ over all of patch δ, the second integral is from the centre of wall patch δ over all of wall patch γ and the last term is evaluated from the centre of patch γ to the centre of patch δ.

All of the components of $\mathscr{M}^{\mathrm{W}}$ have now been specified. The interactions involving integrals over wall patch surfaces are evaluated numerically during the course of a simulation using a nine-point Gaussian quadrature.

REFERENCES

Arp, P. A. & Mason, S. G. 1977 The kinetics of flowing dispersions. VIII. Doublets of rigid spheres (theoretical). *J. Colloid Interface Sci.* **61**, 21–43.

Blake, J. R. 1971 A note on the image system for a stokeslet in a no-slip boundary. *Proc. Camb. Phil. Soc.* **70**, 303–310.

Blanc, R., Belzons, M., Camoin, C. & Bouillot, J. L. 1983 Cluster statistics in a bidimensional suspension: comparison with percolation. *Rheol. Acta* **22**, 505–511.

Bossis, G. & Brady, J. F. 1984 Dynamic simulation of sheared suspensions. I. General method. *J. Chem. Phys.* **80**, 5141–5154.

Bossis, G. & Brady, J. F. 1987 Self diffusion of Brownian particles in concentrated suspensions under shear. *J. Chem. Phys.* **87**, 5437–5448.

Bouillot, J. L., Camoin, C., Belzons, M., Blanc, R. & Guyon, E. 1982 Experiments on 2-D suspensions. *Adv. Colloid Interface Sci.* **17**, 299–305.

Brady, J. F. & Bossis, G. 1985 The rheology of concentrated suspensions of spheres in simple shear flow. *J. Fluid Mech.* **155**, 105–129.

Brady, J. F., Phillips, R. J., Lester, J. C. & Bossis, G. 1988 Dynamic simulation of hydrodynamically interacting suspensions. *J. Fluid Mech.* **195**, 257–280.

Brenner, H. 1961 The slow motion of a sphere through a viscous fluid towards a plane surface. *Chem. Engng. Sci.* **16**, 242–251.

Cox, R. G. & Brenner, H. 1967 The slow motion of a sphere through a viscous fluid towards a plane surface. II. Small gap widths, including inertial effects. *Chem. Engng Sci.* **22**, 1753–1777.

Dean, W. R. & O'Neill, M. E. 1963 A slow motion of viscous liquid caused by the rotation of a solid sphere. *Mathematika* **10**, 13–24.

Durlofsky, L. 1986 Topics in fluid mechanics: I. Flow between finite rotating disks. II. Simulation of hydrodynamically interacting particles in Stokes flow. PhD thesis, Massachusetts Institute of Technology.

Durlofsky, L. & Brady, J. F. 1987 Analysis of the Brinkman equation as a model for flow in porous media. *Phys. Fluids* **30**, 3329–3341.

Durlofsky, L., Brady, J. F. & Bossis, G. 1987 Dynamic simulation of hydrodynamically interacting particles. *J. Fluid Mech.* **180**, 21–49.

Gadala-Maria, F. A. 1979 The rheology of concentrated suspensions. PhD thesis, Stanford University.

Ganatos, P., Pfeffer, R. & Weinbaum, S. 1980*a* A strong interaction theory for the creeping motion of a sphere between plane parallel boundaries. Part 2. Parallel motion. *J. Fluid Mech.* **99**, 755–783.

Ganatos, P., Weinbaum, S. & Pfeffer, R. 1980*b* A strong interaction theory for the creeping motion of a sphere between plane parallel boundaries. Part 1. Perpendicular motion. *J. Fluid Mech.* **99**, 739–753.

Ganatos, P., Weinbaum, S. & Pfeffer, R. 1982 Gravitational and zero-drag motion of a sphere of arbitrary size in an inclined channel at low Reynolds number. *J. Fluid Mech.* **124**, 27–43.

Goldman, A. J., Cox, R. G. & Brenner, H. 1967*a* Slow viscous motion of a sphere parallel to a plane wall. I. Motion through a quiescent fluid. *Chem. Engng Sci.* **22**, 637–651.

Goldman, A. J., Cox, R. G. & Brenner, H. 1967*b* Slow viscous motion of a sphere parallel to a plane wall. II. Couette Flow. *Chem. Engng Sci.* **22**, 653–660.

Happel, J. & Brenner, H. 1973 *Low Reynolds Number Hydrodynamics*, 2nd edn. Noorhoof.

Ho, B. P. & Leal, L. G. 1974 Inertial migration of rigid spheres in two-dimensional unidirectional flows. *J. Fluid Mech.* **65**, 365–400.

Jeffrey, D. J. & Onishi, Y. 1984 Calculation of the resistance and mobility functions for two unequal rigid spheres in low-Reynolds-number flow. *J. Fluid Mech.* **139**, 261–290.

Kim, S. & Mifflin, R. T. 1985 The resistance and mobility functions of two equal spheres in low-Reynolds-number flow. *Phys. Fluids* **28**, 2033–2045.

Ladyzhenskaya, O. A. 1963 *The Mathematical Theory of Viscous Incompressible Flow.* Gordon & Breach.

Leighton, D. & Acrivos, A. 1986 Viscous resuspension. *Chem. Engng Sci.* **41**, 1377–1384.

Leighton, D. & Acrivos, A. 1987 The shear-induced migration of particles in concentrated suspensions. *J. Fluid Mech.* **181**, 415–439.

Liron, N. & Mochon, S. 1976 Stokes flow for a Stokeslet between two parallel flat plates. *J. Engng Maths* **10**, 287–303.

Maude, A. D. 1961 End effects in a falling-sphere viscometer. *Brit. J. Appl. Phys.* **12**, 293–295.

O'Brien, R. W. 1979 A method for the calculation of the effective transport properties of suspensions of interacting particles. *J. Fluid Mech.* **91**, 17–39.

O'Neill, M. E. 1964 A slow motion of viscous liquid caused by a slowly moving solid sphere. *Mathematika* **11**, 67–74.

O'Neill, M. E. 1968 A sphere in contact with a plane wall in a slow linear shear flow. *Chem. Engng Sci.* **23**, 1293–1298.

O'Neill, M. E. & Stewartson, K. 1967 On the slow motion of a sphere parallel to a nearby plane wall. *J. Fluid Mech.* **27**, 705–724.